Journal of Materials Research and Technology 37 (2025) 493–503

Contents lists available at ScienceDirect

Journal of Materials Research and Technology

journal homepage: www.elsevier.com/locate/jmrt

In-situ aluminum 7075 metal matrix composites development for additive friction stir deposition

Huan Ding *, Selami Emanet, Saeid Zavari, Tristan D. Thai, Yehong Chen, Ehsan Bagheri, Shengmin Guo **

Department of Mechanical and Industrial Engineering, Louisiana State University, Baton Rouge, 70803, LA, USA

ARTICLE INFO

Keywords:
Powder metallurgy
Al7075 composite
Additive friction stir deposition
In-situ alloying

ABSTRACT

Al7075 equivalent aluminum + Al_2O_3 metal matrix composite (G7D) feedstock tailored for Additive Friction Stir Deposition (AFSD) was successfully produced using the powder metallurgy and hot extrusion process. Two types of feedstocks with different densities, categorized as High Porosity (HP) and Low Porosity (LP) rods, were AFSD deposited to evaluate their performances. High-quality and fully dense AFSD samples were successfully deposited using both HP and LP rods. The microstructure, grain size distribution, and hardness were evaluated in the as-deposited AFSD samples. The deposited G7D exhibited complex material flow, but deposition parameters had minimal impacts on the flow patterns. During the AFSD process, ceramic particles (Al_2O_3) were evenly dispersed in the matrix. The use of elemental powders rather than pre-alloyed powders allows the low-melting-point metal Zn in the powder mix to form a liquid-phase diffusion pathway during hot extrusion/AFSD, improving the wettability of Al_2O_3 particle surfaces and significantly strengthening the connection between the aluminum matrix and the Al_2O_3 particles. It shows the significant potential of AFSD in fabricating Aluminum Metal Matrix Composites (AMMC) for producing high-quality AMMC components with comparable or superior performance to those made by conventional methods.

1. Introduction

Aluminum alloys are widely used engineering materials due to their lightweight and excellent mechanical properties. In particular, 7000 series aluminum alloys exhibit exceptionally high strength, toughness and excellent resistance to stress corrosion cracking, making them the preferred materials in the aerospace and automotive industries [1–11]. However, with the development of industrial demands, pure aluminum alloys can no longer meet current application requirements. Aluminum Metal Matrix Composites (AMMC) have become a valuable addition to the field of new materials for high-performance applications. AMMCs combine the ductility and toughness of aluminum alloy with the high strength and modulus of ceramics, resulting in higher fracture strength and the ability to function at high temperatures [12–16]. This has greatly attracted the attention of researchers. In fact, numerous studies have highlighted the benefits of AMMCs in detail [9,15–17]. Commonly used reinforcement particles such as Al_2O_3 [18, 19], SiC [20], B_4C [21], TiC [22,23], TiO_2 [24, 25], TiB_2 [26], and graphite [27] have been incorporated into aluminum alloys to produce AMMCs with superior properties. Conventional AMMC processing methods include Stir Casting (SC) [28] and Powder Metallurgy (PM) [29]. Each of these methods has its own advantages and disadvantages. The most prominent issue is that, although these fabrication processes are simple, the final performance of the AMMCs is significantly affected by many factors such as ceramic particle size, processing parameters, and temperature, leading to problems such as uneven particle distribution and insufficient wetting between the reinforcement and the matrix. Also, it is hard to produce large sized homogenous AMMC parts based on these two methods.

Friction Stir Deposition (FSD) represents a novel Additive Manufacturing (AM) technique that functions as a solid-state severe plastic deformation (SPD) process. The major FSD method currently in use is Additive Friction Stir Deposition (AFSD), where rods are typically used as the feedstock. Apart from rod shaped feedstock, wire-based friction stir additive manufacturing (W-FSAM) has also emerged [30–32], which utilizes a continuous feeding system to enable the fabrication of large-scale components. The FSD method incorporates

* Corresponding author.
** Corresponding author.
E-mail address: hding3@lsu.edu (H. Ding).

https://doi.org/10.1016/j.jmrt.2025.05.258
Received 21 February 2025; Received in revised form 1 May 2025; Accepted 30 May 2025
Available online 4 June 2025

additive manufacturing principles by softening raw materials through frictional heat and depositing them layer by layer onto target regions [33–36].

Since the FSD process does not involve metal melting, fatal defects such as hot cracking, chemical composition nonuniformity, porosity, and columnar grain structures that may occur in traditional fusion-based AM processes can be effectively avoided. Another significant advantage of FSD is its ability to achieve ultrafine grains (~5 μm) and uniform material flow. The strength of AMMCs partially depends on the size of the reinforcement phase particles, their distribution within the matrix, and their bonding with the matrix. During the FSD process, significant material flow results in thorough mixing promotes uniformity, heals cracks, fills voids, and establishes excellent interfacial bonding. Consequently, AFSD presents itself as a highly potential collaborator for advancing AMMCs.

However, progress in AMMC material development research related to AFSD and W-FSAM has been remarkably slow. As an emerging technology, most researchers are currently focused on studying commercially available alloy materials, with a limited exploration into alloy composition optimization and redesign. In particular, there is currently a lack of direct research on AMMC materials using the W-FSAM technique. This may be attributed to the fact that in W-FSAM, the primary source of heat input is the friction between the tool pin and the substrate, which may lead to excessive jamming of wire inside the tool. In contrast, the AFSD process generates heat primarily from the friction between the tip of the feedstock rod and the substrate. The large sized rods are designed to take large downward force during the deposition process. Additionally, the tool in AFSD is typically equipped with a cooling system, which helps maintain a lower tool temperature and prevents metallurgical bonding between the AMMC material and the tool. Therefore, at present, the rod-based AFSD process is more suitable for the fabrication of AMMCs. There are indeed some studies attempting to explore from the perspective of customized materials, such as Yoder et al. [34] tried to use the scrap automotive Al chips as the raw material to form the AFSD feedstock with the cold press. It preliminarily demonstrated that AFSD has the capability to deposit porous feedstocks into fully dense components. Additionally, the authors believe that AFSD holds great potential for material recycling and energy consumption reduction. Calvert et al. [37] investigated the tensile properties of WE43 Mg alloy AFSD coatings using powder as feedstock. It was found that the interlayer bonding in the deposited samples was poor, which reduced the mechanical properties. J. Lopez et al. [38] filled Graphite nanoplatelets (GNPs) powder into the hollow AFSD Al6061 feedstock for deposition. Although they successfully deposited this AMMC, the cross-sectional SEM images provided by the authors reveal that the distribution of reinforcement particles is uneven. V. Mani [39] also employed a similar method (powder in hollow rod) to deposit Al6061–B_4C composites and also had a distribution issue. G. G. Stubblefield et al. [40] directly placed copper wire at the center of the feedstock and employed Smoothed Particle Hydrodynamics (SPH) simulations of AFSD to elucidate the deposition mechanics. The results revealed a significant difference in the Cu distribution between the advancing and retreating sides of the deposited sample. Wu et al. [41] combined nanodiamonds and Al6061, and successfully coated the composite to a soft substrate. Those authors also investigated the microstructure evolution of the as-deposited sample.

Currently, most research on composite material development involves directly adding reinforcement phase powders into hollow AFSD feedstock rods, which often results in uncontrollable composition, uneven deposition, and low deposition quality. The ideal AFSD AMMC feedstock should be a solid rod, a form that has been proven to deliver the highest deposition quality. Traditional powder metallurgy processes can ensure uniform mixing of reinforcement particles with the aluminum alloy matrix, but due to mold limitations, producing sufficiently long rods is challenging. This necessitates the use of hot extrusion processes to convert bulk materials into rods. This provides a conceptual framework for the development of the in-situ alloyed AMMC feedstock investigated in this paper.

In this study, we reported preparing in-situ alloying AMMC feedstocks for AFSD technology using hot extrusion and evaluated the AFSD deposited AMMC samples. By using elemental powders instead of pre-alloyed powders, the liquid-phase pathways provided by low-melting-point metal elements facilitated in-situ alloying and improved the wettability of reinforcement particles. The results indicate that a fully dense AMMC composite can be produced even with high-porosity AFSD feedstocks through appropriate parameter optimization. This method can not only be adapted for other aluminum alloy composite designs in the future but also facilitate compositional optimization for other high melting point alloys such as carbon steel, nickel-based alloys, and high-entropy alloys. This will significantly accelerate the development of high quality AMMC parts enabled by the AFSD technology.

2. Materials and method

The raw pre-mixed Al7075 equivalent aluminum + Al_2O_3 metal matrix composite powders (G7D) were purchased from GAMMA ALLOYS (Valencia, CA 91355, USA). The G7D powder included 1 % nano-scale Al_2O_3 particle, 10 % micro-scale Al_2O_3 particle and the Al7075 equivalent element powder (Al, 2.5 % wt Mg, 9.5 % wt. Zn, 1.5 % wt. Cu pure powder). Alumina particles have been uniformly distributed over the metal powder surfaces.

To prepare G7D feedstock rods compatible with the AFSD machine, hot extrusion molding was employed. The G7D powder was first pre-compacted at a temperature of 400 °C and a pressure of 100 MPa. Compaction was performed under both vacuum and atmospheric conditions. Atmospheric compaction is simple to perform. However, due to the large amount of trapped air, the compacts have a lower density than the compacts produced under vacuum. The compacted bulk materials, low density/high porosity ones produced under atmospheric compaction and high density/low porosity ones produced under vacuum compaction, were then heated to 430 °C and extruded through a specific mold (extrusion ratio ~ 22:1) to produce standard AFSD feedstock (9.5 mm × 9.5 mm square bars), as shown in Fig. 1.

A commercial L3 machine from MELD Manufacturing Corporation (USA) was then used in this study. The working principle of MELD has been thoroughly explained in previous works and will not be introduced here. Fig. 1 also illustrates the fundamental printing process of AFSD. In this study, the printing parameters are as follows: Spindle rotation speed of 200 RPM, layer thickness of 1.5 mm, feeding rate of 127–178 mm/min, and traversing speed of 137 mm/min. The applied downward force is about 6.7–8.9 kN. To enable the AFSD deposition process, the surface

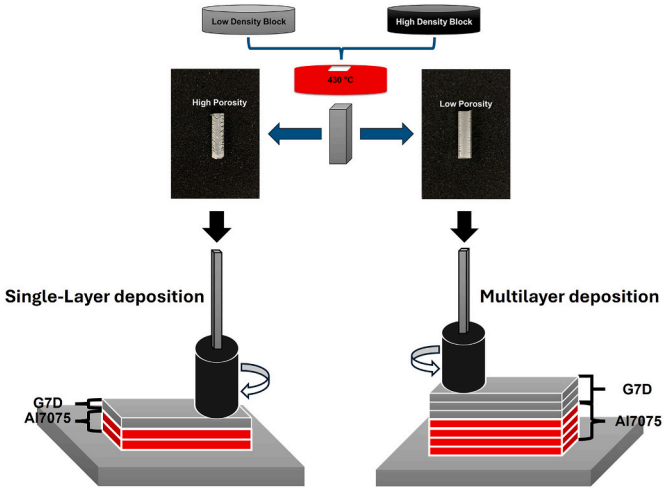

Fig. 1. The procedure of making two different G7D AFSD samples.

of the feedstock rod is coated with a thin layer of graphite to act as a lubricant. The sample detailed information is also shown in Table 1.

The samples, once deposited, were subsequently sectioned using wire Electrical Discharge Machining (EDM). The cross-section, which is parallel to the feeding direction, was sectioned. These were the designated surfaces for analyzing the microstructure, phase structure, composition distribution, and microhardness.

All sample surfaces were mechanically roughly polished using SiC sandpapers, progressing in grit from 400, 600, 800, and 1000. Afterward, they were polished with DIAMAT polycrystalline diamond polishing pads (6 μm, 3 μm, and 1 μm) to attain a mirror surface. The final polishing process was performed on a vibratory polisher (Pace Technologies GIGA Vibratory Polisher) for 5 h in a pulse mode with 35 nm silica suspension.

Scanning Electron Microscopy (SEM) and Energy Dispersive Spectroscopy (EDS) were performed on the ThermoFisher Helio G5 Xe PFIB/SEM system. Both the EDS mapping and Electron Backscatter Diffraction (EBSD) mapping were performed at 20 kV and 3.2 nA with an EDS/EBSD detector on the same PFIB/SEM system. Grain size was also calculated from the EBSD data as the equivalent circular diameter. MicroCT was performed at a Heliscan MicroCT (Mark II) system with tungsten filament. The working voltage and current are 140 KV and 55 μA. Microhardness tests were performed on the specimens using a CM-802 AT microhardness tester, with a test load of 500 gf and a dwell time of 15 s.

3. Results

3.1. Hot extruded rods

Numerous studies have summarized the technical features of AFSD [4,35,36,42,43], with the most compelling being large-scale fabrication, ultrafine grains, and uniformity of printed samples. Therefore, this study uses both high-quality and low-quality feedstock rods to further validate the in-situ alloying process and the final quality of AFSD AMMC samples.

As shown in Fig. 1, two types of hot extrusion rods were prepared, which are High Porosity (HP) G7D rods and Low Porosity (LP) G7D rods. Both types of rods utilized the same hot extrusion process, with the key distinction lying in the condition of the initial compressing process. The HP rod's block was pressed under standard atmospheric conditions, containing numerous closed pores internally. During the hot extrusion process, the pressure difference between the closed pores and the external atmosphere led to the formation of a popcorn-like structure on the rod's surface. When the powder is compressed under vacuum conditions, the internal closed pores are significantly reduced but cannot be completely eliminated. As a result, a small number of cracks remain in the final LP rod. Just as shown in Fig. 2 (a) and (c). To further quantify the porosity of the different rods, Avizo was used to calculate the volume of the crack after the MicroCT scanning, and the crack density of the HP and LP rods is 23.08 % and 9.24 % respectively.

It is noteworthy that the cross-sections of the two rods show distinct characteristics. The crack area width in the HP rod is about 1.9 mm, while the width in the LP rod is way far less (~0.5 mm). A significant amount of white phase was observed at the edges (~1.6 mm) of the LP rod scan, whereas no such feature was present in the HP rod. During the MicroCT scanning process, the sample continuously rotates to facilitate the acquisition of its 3D information. Due to the considerable size of the two rods (9.5 mm × 9.5 mm), X-rays may lose resolution and certain features when traversing through the sample in the forward direction (Fig. 3(a)). Distinct features at the thinner edges only become visible when the sample rotates to a specific angle, as illustrated in Fig. 3(b). During SEM/EDS analysis, the bright white phase was observed both at the edges and in the central areas of the LP rods. This confirms that the feature loss in the central area of the LP rods is due to the CT scan process. However, due to space limitations, only the EDS spectrum of the bright white phase at the edges is presented in Fig. 2 (e). In the EDS map (The red dashed rectangle in the edge area), it can be observed that the Al_2O_3 particle (Black dot in Fig. 2 (e) and it was overlapped with O distribution) is evenly distributed in the matrix. The primary constituent elements of the white phase are Cu, Zn, and Fe, which means a significant partial alloying process occurred in the LP rods during the compressing and hot extrusion process. This alloying process was not detected in the HP rods, and the reasons will be discussed in subsequent sections.

Fig. 4 shows the microhardness of the center area from two rods. Hardness measurements were conducted at ten random points within the central areas of the two rods, resulting in values of 134.1 ± 1.2 HV for the HP rod and 135.4 ± 1.3 HV for the LP rod. The microhardness of both rods is nearly identical because they share the same powder matrix. Thus, the microhardness in the dense regions mainly originates from the in-situ Al7075 powder itself.

Table 1
AFSD Sample printing information.

Sample Type	Sample Code	Layer Thickness	Feed rate	Travel Speed	Tool Rotation
Single layer	SL5	1.5 mm	**127 mm/min**	137 mm/min	200 RPM
	SL5.5	1.5 mm	**140 mm/min**	137 mm/min	200 RPM
	SL6.5	1.5 mm	**165 mm/min**	137 mm/min	200 RPM
Multiple layer	ML7.0	1.5 mm (**3 layer**)	**178 mm/min**	137 mm/min	200 RPM

3.2. Single layer deposition

Fig. 5 shows the as-deposited sample with different feed rates and the reaction force during the first 2 inches of deposition. HP rods were used as AFSD feedstock materials for single-layer deposition, and the primary purpose of the single-layer experiment was to optimize AFSD parameters to lay the foundation for subsequent multi-layer printing while also studying the in-situ alloying process within the single layer. Since HP rods were used, defects such as pores and cracks in the rods led to insufficient material feeding when the feeding rod initially exerted pressure. Therefore, the primary parameter significantly affecting deposition quality is the feed rate. This section primarily focuses on the feed rate as the main subject of parameter study.

It was observed that the deposition quality of the latter section of the samples was superior, leading to a focus on investigating the microstructure and properties of the Insufficiently Fed Zone (IFZ) area to obtain a better understanding of mass flow and optimize the process in the future. As shown in Fig. 5 (a), (b), and (c), with an increase in feed rate, the IFZ area gradually shrinks, and the quality of the deposited surface is improved.

Due to the lack of sufficient sintering time and solid-state diffusion, it is expected that the strength of the hot-extruded rod is lower, resulting in lower applied downward force during the AFSD process compared to using solid Al7075 T6 rods, as shown in Fig. 5 (d). A comparison of reaction force in the first 2-inch traveling during the AFSD, including the IFZ area, reveals that the tested feed rate range has minimal impact on downward force and exhibits a consistent trend. During the AFSD deposition process, the downward force applied to the hot-extruded rod first increases and then becomes stabilized. This is because, at the initial stage of deposition, increasing the downward force aids in further densification of the rod, leading to a reduced feed rate. With the progression of the deposition process, the densification of subsequent rods improves. Finally, the rods reach a stabilized feed rate and a stabilized downward force.

To investigate the depth of the IFZ area and the internal density of

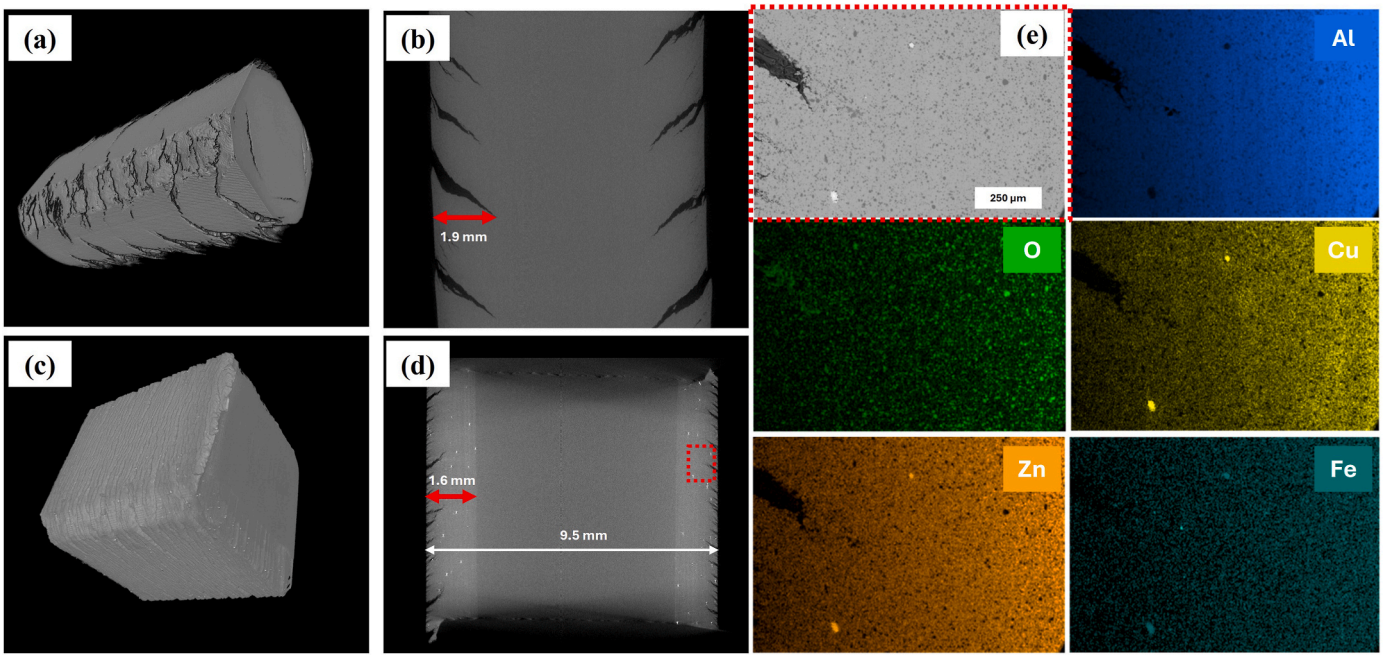

Fig. 2. Micro CT results for different rods (a) HP rod (b) HP - Cross section (c) LP rod (d) LP - Cross section (e) EDS mapping in the side of LP rod.

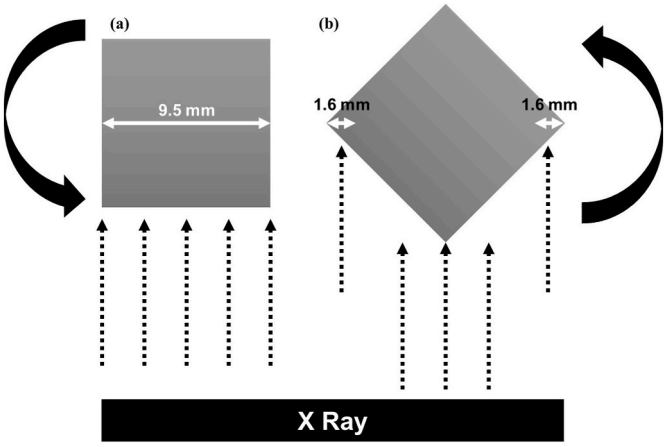

Fig. 3. Micro CT scanning strategy.

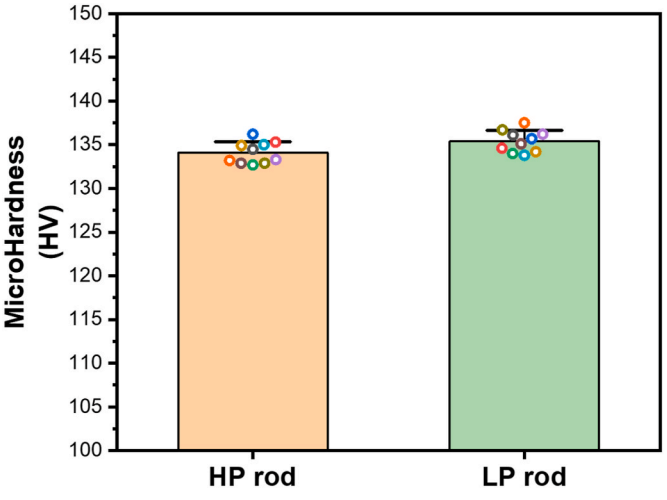

Fig. 4. The Microhardness HP rod and LP rod.

the AFSD samples (Center area), X-ray CT was employed. The results are shown in Fig. 6. In the SL5.0 sample, the average depth of the IFZ area (indicated by the red double arrow) is 1.12 ± 0.05 mm. In the SL6.5 sample, the average depth of the IFZ area is only 0.64 ± 0.13 mm. This indicates that the IFZ is a portion of the AFSD layer thickness and has a solid underlayer. IFZ was effectively filled as the feed rate increased. Excluding the IFZ area, all other deposited areas in both samples are fully dense without any visible pores or cracks.

Fig. 7(a–c) shows the cross-section area in the IFZ of the SL5.0, SL5.5, and SL6.5, respectively. The cross-section reveals nearly identical characteristics, featuring black areas at both the top and bottom (White dashed area). And gray areas occupied the remaining area. This indicates that the tested feed rate range has no significant impact on the HP rod's mass flow during the friction stir deposition process. To visually highlight the distinctions between the black and gray areas, a 2 mm × 1.25 mm rectangular area (red dashed rectangle area) at the tip of the black area below was chosen for hardness testing, as illustrated in Fig. 7. The average hardness of the dark area in the SL5.0, SL5.5, and SL 6.5 were 114.6 ± 3.1 HV, 116.3 ± 2.2 HV, and 117.1 ± 1.9 HV, respectively. The average hardness of the white area in the SL5.0, SL5.5, and SL 6.5 were 88.7 ± 2.6 HV, 87.8 ± 3.0 HV, and 87.4 ± 1.8 HV, respectively. Previous studies have confirmed that after the AFSD process, the hardness of the as-deposited Al7075 sample decreases to a minimum, of approximately 80–90 HV [4,33]. This reduction is attributed to the transformation and coarsening of strengthening phases η' in the matrix. The hardness range is similar to that of the gray area in this study, suggesting that the gray area primarily consists of pure Al7075 alloy with little to no Al_2O_3.

To further investigate the distribution of Al_2O_3, an EDS scan was performed at the tip. The results are shown in Fig. 8. As the data showed redundancy in the SL5.0, SL5.5 and SL6.5, only the EDS elemental mapping for the SL5.5 sample is displayed here. EDS mapping has verified that the black areas in Fig. 7 (a), (b), and (c) result from a high concentration of Al_2O_3. Aluminum oxide particles are uniformly dispersed throughout the matrix. In the gray area, no micron-scale Al_2O_3 particles are detected, with only secondary phase particles related to Mg and Fe observed. Additionally, the SEM-BSE images reveal numerous ultra-fine bright white phases distributed in the black area, and primarily consisting of Zn, Mg, and Cu, which is shown in Fig. 8 (b).

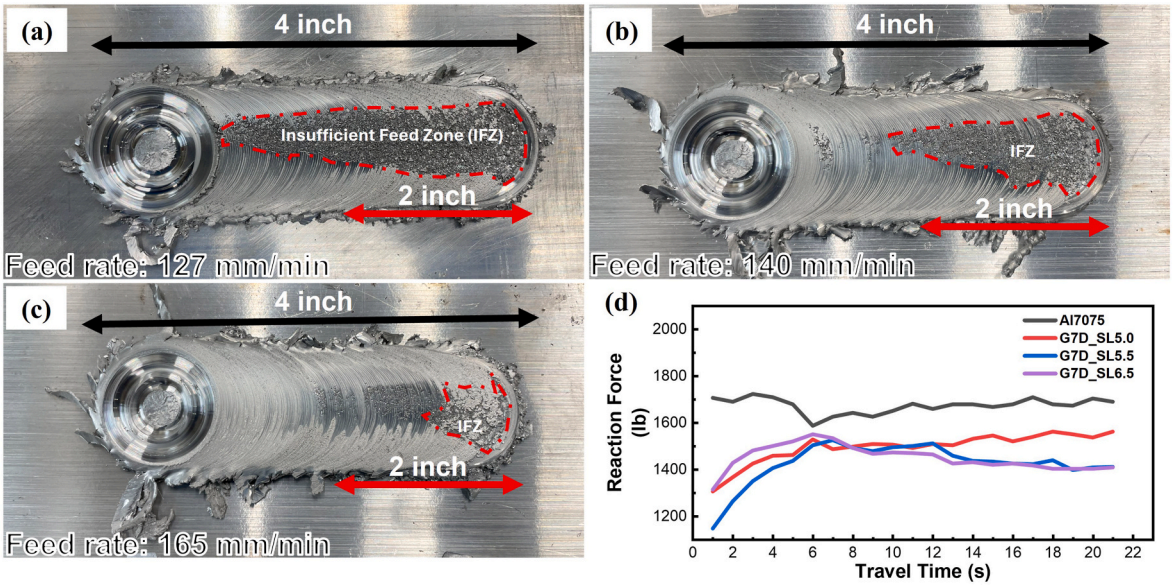

Fig. 5. Single Layer deposition with different feed rates (a) SL5.0: 127 mm/min (b) SL5.5: 140 mm/min (c) SL6.5: 165 mm/min (d) Reaction force for the as-deposited sample.

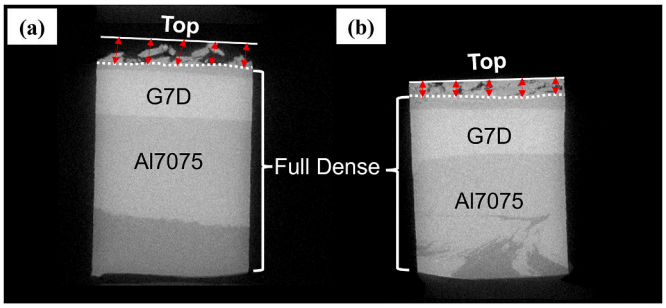

Fig. 6. X-ray CT for Density check (a) SL5.0 and (b) SL6.5.

According to previous studies [4], this phase is identified as the incoherent η phase. A small amount of Fe-related impurity particles was detected, but their size was significantly smaller than the Fe impurity particles in the gray regions.

3.3. Multilayer deposition

The single-layer deposition samples demonstrated the fundamental microstructure and mass flow of the AFSD G7D, providing significant guidance for optimizing printing parameters in multilayer deposition. In the single-layer deposition, increasing the feed rate to 165 mm/min still resulted in a small presence of IFZ on the deposited sample's surface. To enhance printing quality, the feed rate was increased to 178 mm/min in the multilayer deposition. At the same time, the LP rod was adopted as the AFSD feedstock to gain better quality. Fig. 9(a) shows the as-deposited multilayer G7D sample ML7.0. It exhibited a high-quality

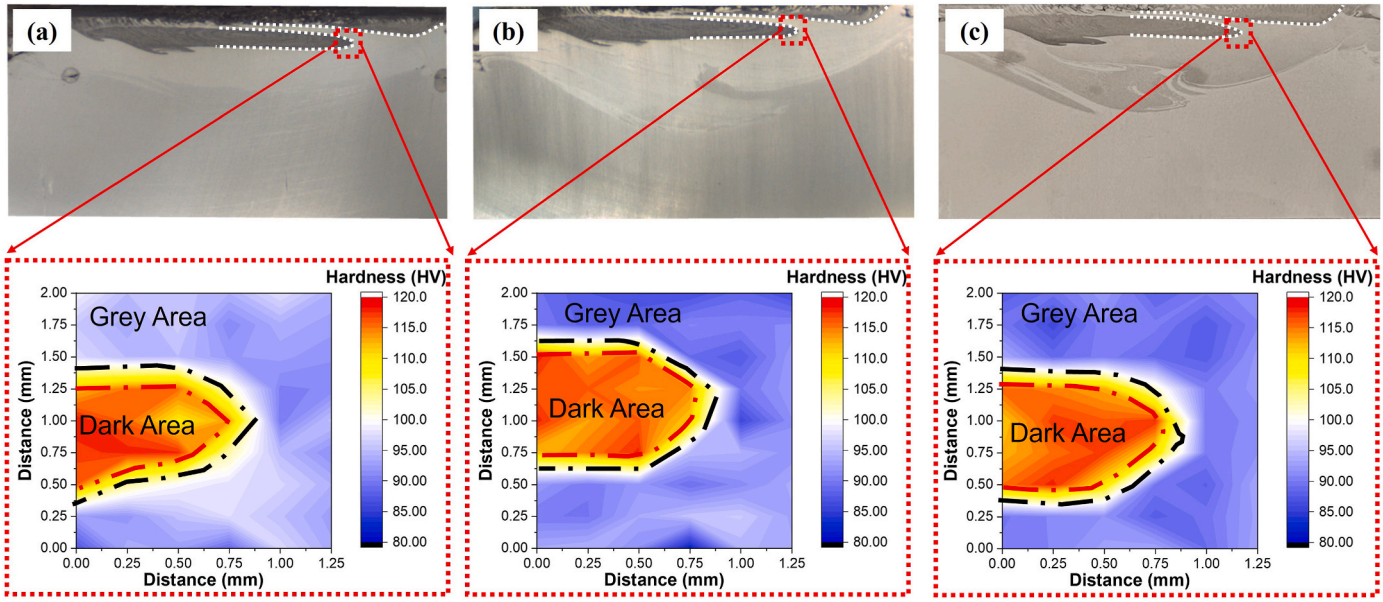

Fig. 7. Cross section of AFSD sample (a) SL5.0 (b) SL5.5 (c) SL6.5 and corresponding microhardness map of the partial area.

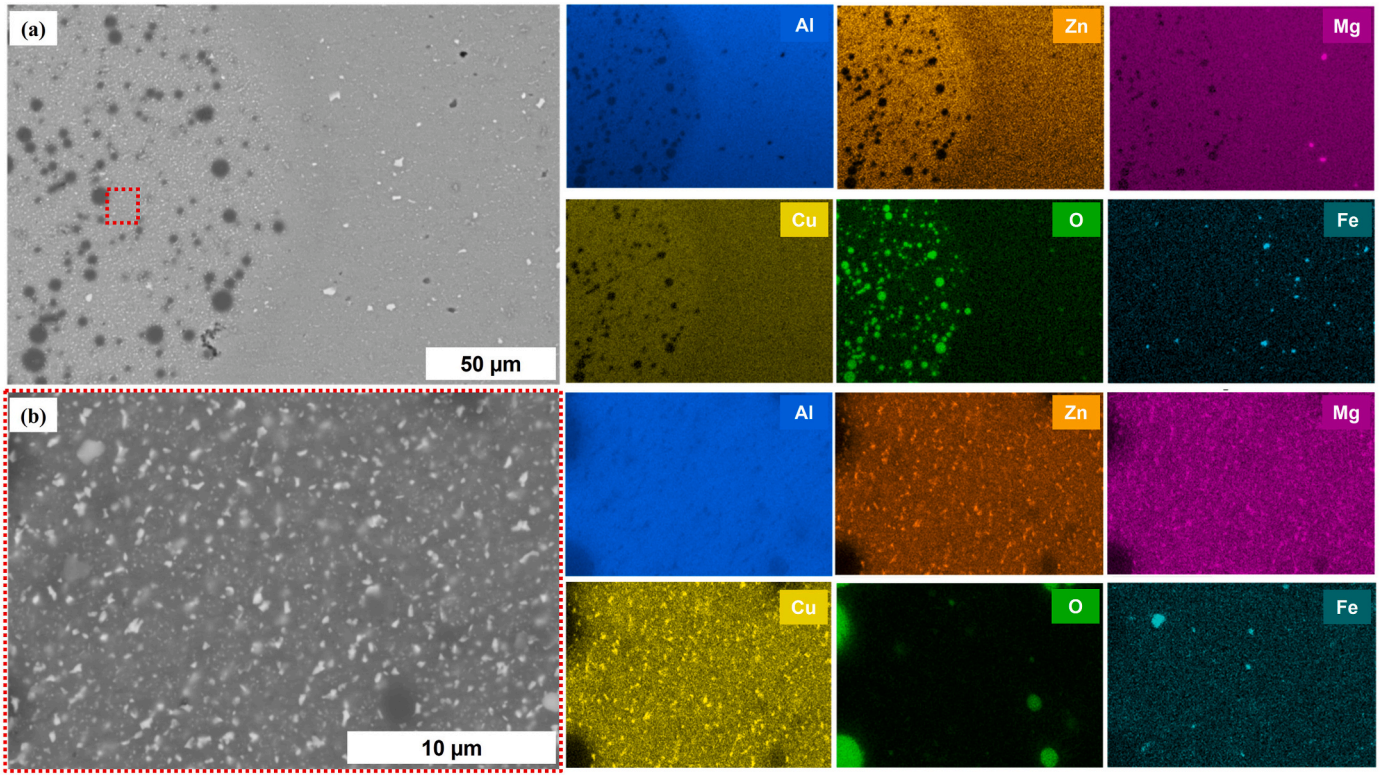

Fig. 8. BSE-EDS mapping for (a) the tip area from SL5.5 sample and (b) the high-magnification of the black area.

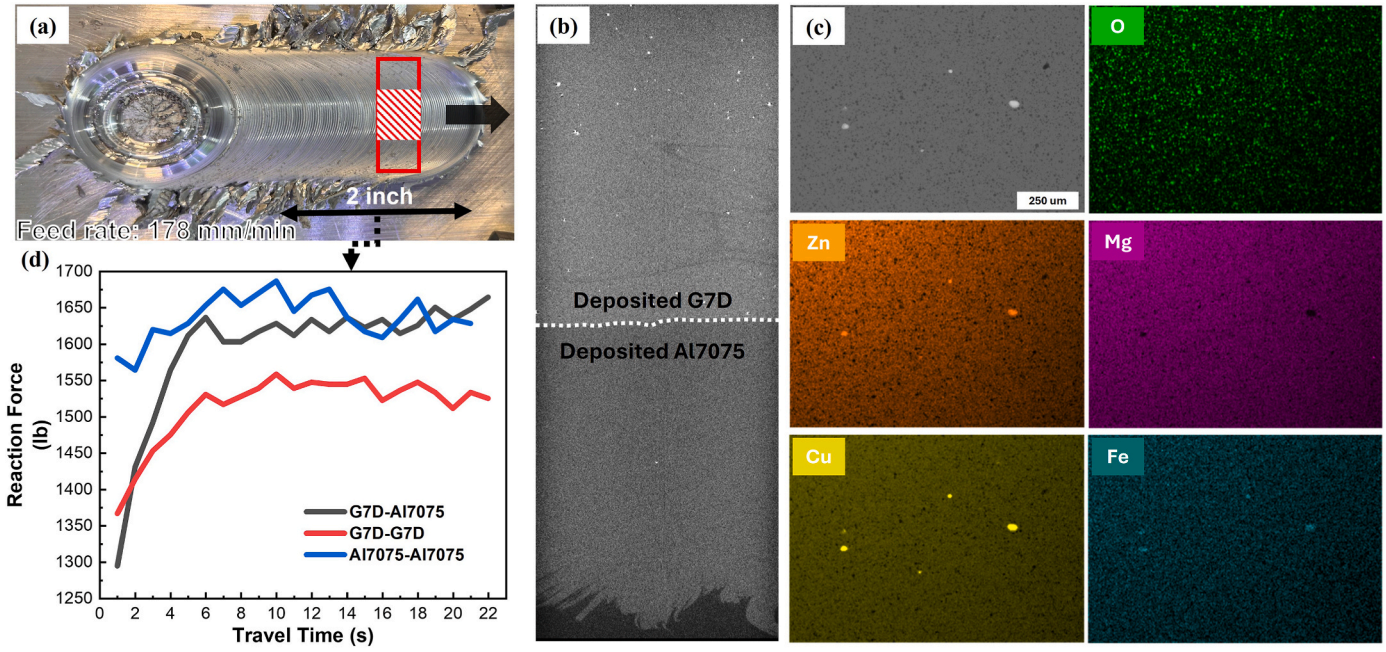

Fig. 9. Multiple layer Deposition sample (ML7.0) (a) As-deposited 3 layer G7D sample, (b) Xray CT scan results of the central area in the as-deposited G7D, (c) BSE-EDS mapping of the as-deposited G7D, and (d) Reaction force curve in the first 2-inch travel during the AFSD process.

surface without any IFZ. Fig. 9(d) illustrates the variation in reaction force over the first 2 inches of different deposition layers. Three typical deposition layers were selected: Al7075 feedstock deposited on an Al7075 substrate (Al7075–Al7075), G7D feedstock deposited on an Al7075 deposition layer (G7D-Al7075), and G7D feedstock deposited on a G7D deposition layer (G7D-G7D). The G7D feedstock exhibits a trend of reaction force initially increasing and then stabilizing, regardless of whether it is deposited on Al7075 or G7D. This behavior is attributed to the low density of the feedstock. The G7D-G7D reaction force is lower than that of Al7075–Al7075 and G7D-Al7075, which is possibly caused by the abundant wear-resistant Al_2O_3 particles in G7D. During the AFSD process, this enhanced friction behavior increases the working temperature, thereby softening the feedstock and reducing the reaction force.

Fig. 9(b) shows the X-ray CT scan image of the red rectangular center

in Fig. 9(a), which includes a total of seven layers of the G7D/Al7075 sample. The white dashed line represents the boundary between the deposited G7D and Al7075. A total of 1800 cross-sectional CT scan images were produced, with only representative images shown here. The deposited G7D sample shows no visible defects and appears to be nearly fully dense. In contrast to the single-layer G7D sample, the matrix of the multilayer G7D sample exhibits numerous white secondary phases. Therefore, EDS scanning was performed on the matrix, and the results are shown in Fig. 9.

The bright white phases correspond to Zn–Cu–Fe secondary phases, identical in composition to the white secondary phases identified in Fig. 2(e). This means that during the AFSD process, the bright white secondary phases in the LP feedstock did not fully re-dissolve into the matrix but instead were uniformly distributed across the matrix during the stirring process.

Fig. 10(a) shows the cross-section of the deposited sample. To ensure experimental consistency, the selection position of the cross-section aligns with that of the single-layer experiment. The deposited G7D layers still exhibited distinct flow texture, especially in the top layer (marked by white dashed lines), which closely resembled those observed in the single-layer experiment (Fig. 7). As shown in Fig. 10(b), the deposited G7D and Al7075 in the center line (Yellow and black arrow) exhibit average microhardness values of 117.6 ± 1.3 HV and 89.5 ± 2.7 HV, respectively.

Fig. 10(c–e) present the microstructures of the G7D layer and Al7075 layer using SEM-BSE images. It can be observed that Al_2O_3 is uniformly distributed in the G7D matrix, accompanied by numerous fine white secondary phases. In the Al7075 layer, white secondary phase particles are observed to form a network-like structure within the matrix. These network-like regions indicate the presence of grain boundaries (marked by white dashed lines in Fig. 10(e)).

Fig. 10(f) shows the EBSD map of the G7D/Al7075 interface. The upper part corresponds to G7D, the lower part to Al7075, separated by a white dashed line. In the EBSD map, the black areas in the upper part represent Al_2O_3. The EBSD map reveals no significant grain orientation preference, and the grains in the G7D layer are significantly smaller than those in the Al7075 layer. The average grain sizes of G7D and Al7075 are 2.09 ± 0.23 μm and 5.56 ± 0.47 μm, respectively. The restricted grain growth is caused by the pinning effect of Al_2O_3 particles. This suggests that incorporating ceramic particles can refine the grains further and improve the matrix's strength. This topic will be explored further in later sections.

4. Discussion

4.1. The effect of the feedstock and deposition parameter on deposition quality

In this paper, two types of rods were employed to test the deposition quality. The HP rods were primarily used for single-layer experiments, while the LP rods were mainly used for constructing high-quality multilayer AFSD samples. This is because, based on physical principles, the deposition of HP rods is expected to exhibit various defects, making it necessary to use HP rods for single-layer experiments to optimize deposition parameters. The experiments indicate that the feed rate is a key influencing factor. Although tool travel speed and rotation speed might impact deposition quality as well, these aspects are beyond the scope of this paper. Further optimization of these parameters will be explored in future studies.

In the single-layer deposition, it can be observed that the as-deposited sample from the HP rod shows a low surface quality even with a higher feed rate. As shown in Fig. 5 (a)(b)(c), only the central area exhibits a metallic luster, while the sides display a matte texture (cement-like pattern). This phenomenon is more pronounced in the first half of the deposited sample and improves in the latter half, possibly because the low density and strength of the rod at the beginning of deposition prevents G7D from being uniformly deposited onto the substrate. As deposition progresses, the densification and strength of the HP

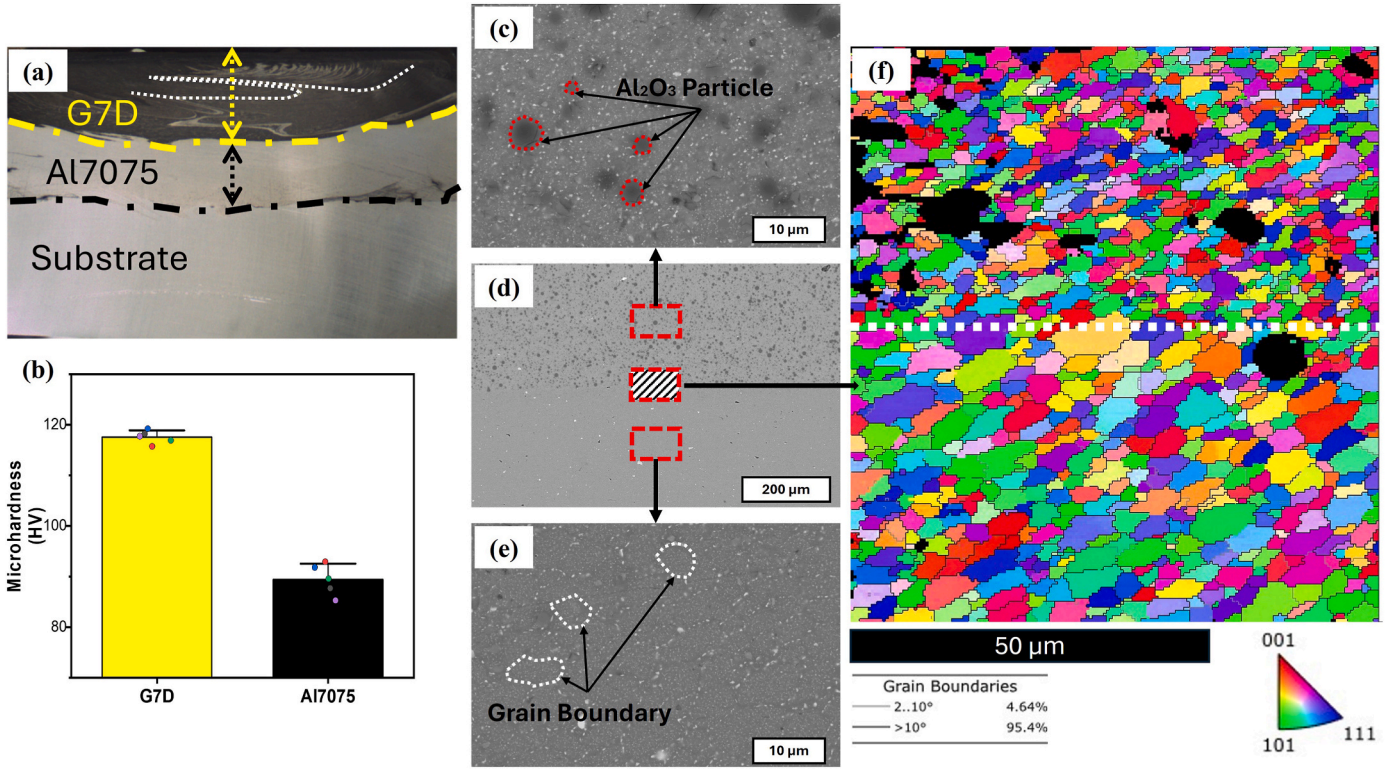

Fig. 10. (a) Cross-section of the as-deposited ML7.0 and Al7075 (b) Microhardness of the ML7.0 and Al 7075 (c) BSE image for as-deposited ML7.0 (d) BSE image for the interface between the ML7.0 and Al7075 (e) BSE image for as-deposited Al7075 (f) EBSD for the ML7.0 and Al7075.

rod improves under high temperature and pressure, enhancing the quality of subsequent deposition. X-ray CT results show that with increasing feed rate, the density of AFSD samples within the IFZ also improves. Due to the inherent defects in the HP rods, AFSD at high feed rates still exhibits minor defects. However, X-ray CT results reveal that most areas of the deposited single-layer G7D are nearly fully dense.

The deposition parameters mainly influence the localized surface roughness of the samples, while their effect on the mechanical properties (microhardness) of the fully dense regions is almost negligible. This is because the strength of the Al alloy matrix decreases to a low level after the AFSD process, with the G7D composite additional strength primarily derived from the hard Al_2O_3 particles. Even with different deposition parameters, it will not significantly break down the Al_2O_3 or re-arrange the particle distribution. Therefore, all three single-layer samples exhibited the same microhardness trends in the composite area.

For the multilayer deposition, both in density and surface smoothness, the ML7.0 samples produced using LP rods demonstrated outstanding performance. The cross-sectional analysis showed a homogeneous distribution of Al_2O_3. A white phase region was observed in the first G7D layer, attributed to the vigorous stirring in the AFSD process, mixing material from the substrate Al7075 layer. Consequently, a portion of pure Al7075 was retained in the first layer of G7D, but such white phase regions were rarely observed in subsequent layers.

4.2. In-situ alloying and strength mechanism in rod and AFSD sample

In-situ alloying mainly relies on changes in temperature and pressure. Therefore, the stages where in-situ alloying occurs are primarily during pre-pressing, hot extrusion, and the AFSD process.

The lowest melting point in the mixed G7D powder is 420 °C (Zn powder). Therefore, during the pre-pressing process (400 °C), a very slow solid-state diffusion and sintering could occur, but in-situ alloying is unlikely to happen on a large scale since the pressing time is short. Especially under non-vacuum compression, there are many pores in the bulk material, and the contact area between the particles is less compared to that in a vacuum-compressed bulk material. During the hot extrusion processes, the processing temperature (430 °C) exceeded the liquidus (420 °C), facilitating liquid-phase sintering and resulting in partial alloying of the rods. Due to the short time of the hot extrusion process and the presence of numerous voids in the HP rod, even if there are liquid phases in the bulk material, in-situ alloying is still unlikely to be completed. This is also why no secondary phase was detected in the MicroCT results in Fig. 2(b). In the LP rod, the number of voids and defects further decreases, and the increased contact area between particles promotes liquid phase sintering and diffusion, ultimately leading to in-situ alloying. As shown in Fig. 2(d), large white phases are the secondary phases related to the Zn, Cu, and Fe elements. Further magnification of the LP rod matrix is shown in Fig. 11(a), displaying the elemental distribution of the matrix particles in the LP rod at high magnification. It can be observed that under the current temperature parameters, the coarsened η-phase (Mg, Zn, Cu) has appeared in the rod, indicating that the in-situ alloying process has been mostly completed during the hot extrusion process.

During the AFSD process, the peak temperature is influenced by the tool rotation rate and travel speed. Ignoring the minor temperature differences between the advancing side and the retreating side, the temperature empirical equation established by Commin et al. [44] can be approximately expressed as:

$$\frac{T}{T_m} = K\left(\frac{\omega^2}{V \times 10^4}\right)^a$$

where T_m is the melting point (°C), ω is the tool rotation rate (RPM) and V is the traverse rate (mm/min). K and a are constant, and the range are between 0.64-0.75 and 0.04–0.06, respectively. For Aluminum [45], K = 0.75 and a = 0.04. According to the phase diagram calculations [2], the melting point of the current Al7075 alloy should be 470 °C. The rotation speed and traverse rate here are 200 RPM and 137 mm/min. So, the AFSD working temperature for the Al7075 should be 310 °C. During the actual printing process, we observed that the substrate temperature

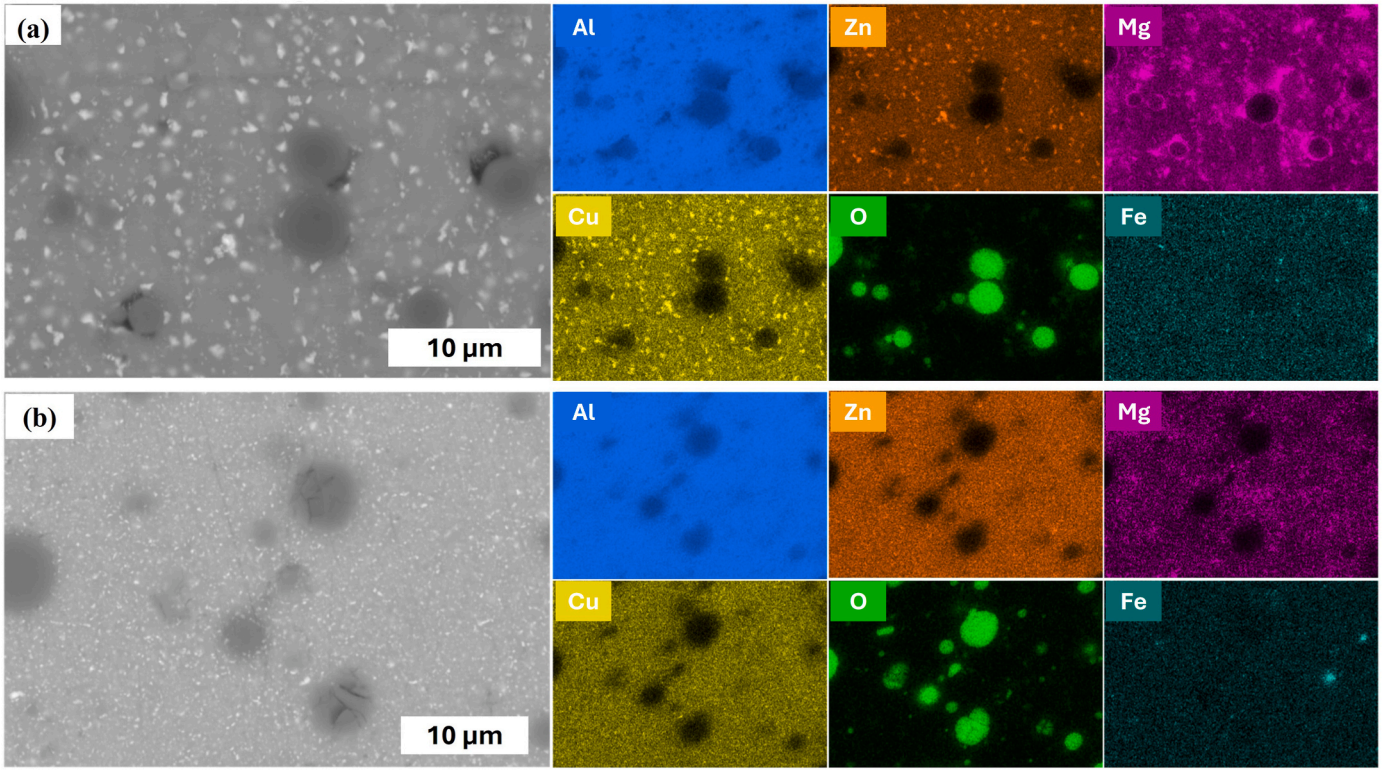

Fig. 11. EDS mapping for (a) LP rod (b) ML7.0.

was approximately 330 °C. Elevated temperatures in precipitation-hardened Al7075 promote the transformation of strengthening η' ($MgZn_2$) phases into non-strengthening η ($MgZn_2$) phases. In Al7000 series alloys, phase evolution follows the sequence: Guinier-Preston (GP) zones → metastable η' → stable η. The η′ phase, formed through solution treatment and aging, begins to coarsen around 300 °C, gradually converting to η and weakening the matrix. This theory is also validated by our previous experimental results [4], where an Al7075 rod with an initial hardness of 180 HV experienced a reduction to 80 HV after undergoing AFSD processing.

Things become interesting with the AFSD G7D alloy. Theoretically, since G7D consists of 89 % Al7075 and 11 % Al_2O_3 particles, it can be approximated that the AFSD working temperature of Al7075 and G7D is similar. This implies that, without considering the reinforcement effect of Al_2O_3 particles, the matrix strength in AFSD G7D would decrease to its minimum (~80 HV). According to our unpublished experimental data, Al_2O_3 particles contribute an approximate 20 HV increase to the matrix (~100 HV). In this work, the AFSD G7D hardness was observed to be around 120 HV. This suggests that the AFSD process contributed to an enhancement in Al matrix strength. This enhancement may be attributed to multiple factors. On one hand, the Al_2O_3 particles further refined the grain size of the matrix, providing grain boundary strengthening. On the other hand, these wear-resistant particles may generate additional heat during friction, thereby increasing the working temperature. As a representative of precipitation-hardened aluminum alloys, the strength of the Al7075 matrix primarily originates from the formation of semi-coherent strengthening η′ phases. Although the EBSD image revealed further grain refinement in the G7D matrix, the magnitude of this change is unlikely to result in a significant difference in strength. The improvement in matrix performance is primarily attributed to the reformation of strengthening phases within the Al matrix.

Fig. 12 shows the Thermo-Calc phase diagram of Al7075. The variation curve of phase C14_Laves (η'/η phase) content with temperature (in purple) is also shown in the figure. With a standard Al7075 deposition condition (~300 °C), the volume fraction of η'/η phase is around 0.065 %. At room temperature, the volume fraction of the η'/η phase is approximately 0.082 %. Only a minimal amount of the η'/η phase dissolves at 300 °C. Whether the matrix is dominated by η′ phase or η phase,

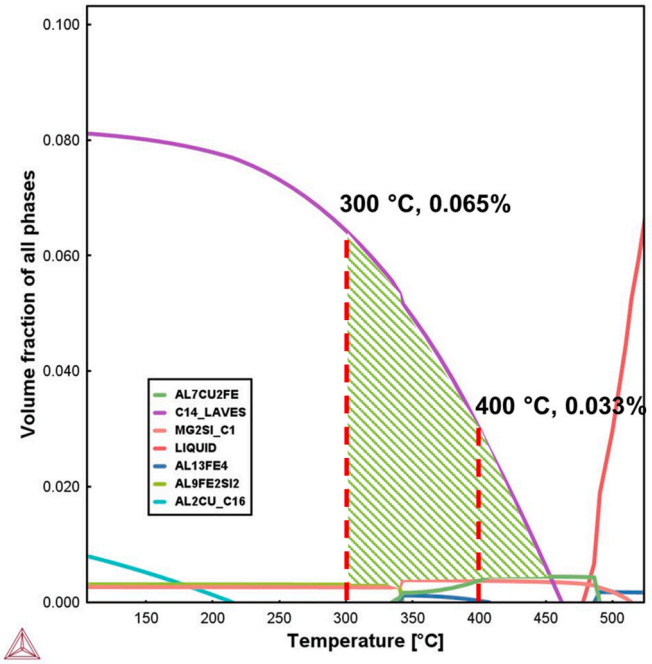

Fig. 12. Al7075 one-axis phase diagram.

the coarsened η phase will ultimately form at 300 °C. The η′ phase first transforms into the η phase along the phase transformation pathway, followed by further growth. The η phase undergoes direct coarsening. The phase evolution significantly compromises the mechanical integrity of the matrix. For the AFSD G7D sample, the additional frictional heat input elevates the deposition temperature. This promotes the dissolution of an increased amount of η'/η phases. A compelling evidence is shown in Fig. 11, where the Mg–Zn–Cu phases (white phases) in LP rods exhibit a significant size reduction after AFSD, demonstrating that these precipitates underwent a dissolution-reprecipitation process. Although the temperature increment cannot be precisely calculated, the enhanced matrix strength indicates an increased η′ phase content of the matrix.

4.3. Bonding between the reinforcement particle and the matrix

An important factor influencing the strength of composite materials is the strength of bonding between the reinforcement particles and the matrix.

To enhance the wettability between Al_2O_3 particles and the matrix, Al7075 elemental powder was used instead of pre-alloyed powder. Since Magnesium (Mg) is reported to diffuse to the aluminum–aluminum oxide interface and to react with Al_2O_3 to form a spinel during the sintering process with the following reaction equation:

$$3\,Mg + 4Al_2O_3 \rightarrow 3MgAl_2O_4 + 2Al$$

This mechanism helps create diffusion pathways between the matrix and Al_2O_3. As a result, it enhances the adhesion between the matrix and Al_2O_3. The distribution of Mg elements in Fig. 11a and b clearly shows the aggregation of Mg near the Al_2O_3 particles. This indicates that Mg successfully wetted the Al_2O_3 particles and established a diffusion channel with the matrix, ultimately enhancing the bonding between the Al_2O_3 particles and the matrix.

The success of this deposition strategy significantly reduced raw material costs, as gas-atomized or water-atomized pre-alloyed powders are generally more expensive than pure elemental powders. Moreover, the use of pre-alloyed powders leads to poor wetting with Al_2O_3 particles because a thin layer of Al_2O_3 oxide film has already formed on the surface of the pre-alloyed powder. Using a mixture of elemental powders significantly mitigates the limitations of using pre-alloyed powders in in-situ processes. For example, due to the pre-existing thin Al_2O_3 oxide layer on the surface of pre-alloyed powders, their wettability with Al_2O_3 particles would be inherently poor. Even after high-temperature hot extrusion and the additive friction stir deposition (AFSD) process, the interfacial bonding between the matrix and Al_2O_3 particles would remain weak, ultimately leading to degraded mechanical properties of the as-deposited material.

5. Conclusion

Through powder metallurgy, hot pressing, and extrusion, we successfully fabricated Al7075 equivalent aluminum + Al_2O_3 metal matrix composite (G7D) feedstock for AFSD. Based on the study of the microstructure and properties of AFSD deposited samples, the following conclusions were drawn.

(1). The High Porosity (HP) rods can be directly used in the AFSD process, and the fully dense sample can be deposited with a high feed rate. The AFSD samples deposited with Low Porosity (LP) rods exhibited excellent performance, including full density, high surface smoothness, and uniform distribution of Al_2O_3 particles.
(2). The microhardness of the base alloy is reduced to a low level after the AFSD process, and the microhardness of the deposited G7D samples is improved by the hard Al_2O_3 particle and it will not be strongly affected by the deposition parameters except the temperature.

(3). The use of non-pre-alloyed powders can promote in-situ alloying through the liquid phase generated by low-melting-point metal element, improving the wettability of Al_2O_3 particles and thereby enhancing the bonding between the hard particles and the matrix.
(4). Powder metallurgy and hot-extruded feedstock preparation strategy provides a new research window for metal-ceramic composite materials design, significantly expanding the material base for AFSD applications.

CRediT authorship contribution statement

Huan Ding: Conceptualization, Methodology, Investigation, Writing – original draft, Writing – review & editing. **Selami Emanet:** Investigation. **Saeid Zavari:** Investigation. **Tristan D. Thai:** Investigation. **Yehong Chen:** Investigation. **Ehsan Bagheri:** Investigation. **Shengmin Guo:** Conceptualization, Writing – review & editing, Funding acquisition.

Data availability

Data will be made available on request.

Funding

This work was supported by the US National Science Foundation under grant number OIA-1946231 and the Louisiana Board of Regents for the Louisiana Materials Design Alliance (LAMDA). SG is also partially supported by the Center for Innovations in Structural Integrity Assurance (CISIA), a National Science Foundation (NSF) Industry/University Cooperative Research Center (Award number 2052810) and an Air Force SBIR program. HD is also supported by the Louisiana Board of Regents with the award number AWD-AM241378.

Declaration of competing interest

The authors declare that they have no known competing financial interests or personal relationships that could have appeared to influence the work reported in this paper.

References

[1] Montero Sistiaga ML, Mertens R, Vrancken B, Wang X, Van Hooreweder B, Kruth JP, Van Humbeeck J. Changing the alloy composition of Al7075 for better processability by selective laser melting. J Mater Process Technol 2016;238:437–45. https://doi.org/10.1016/j.jmatprotec.2016.08.003.
[2] Ding H, Zeng C, Raush J, Momeni K, Guo S. Developing fused deposition modeling additive manufacturing processing strategies for aluminum alloy 7075: sample preparation and metallographic characterization. Materials (Basel) 2022;15(4). https://doi.org/10.3390/ma15041340.
[3] Li G, Jadhav SD, Martín A, Montero-Sistiaga ML, Soete J, Sebastian MS, Cepeda-Jiménez CM, Vanmeensel K. Investigation of solidification and precipitation behavior of Si-modified 7075 aluminum alloy fabricated by laser-based powder bed fusion. Metall Mater Trans A 2021;52(1):194–210. https://doi.org/10.1007/s11661-020-06073-9.
[4] Ding H, Bhandari U, Zhu P, Bagheri E, Zavari S, Chen Y, Mu Y, Wang Y, Guo S. Peak microhardness recovery via T6 heat treatment with extremely soft annealed Al7075 feedstock in additive friction stir deposition. J Mater Res Technol 2024;32:2993–3003.
[5] Momeni K, Neshani S, Uba C, Ding H, Raush J, Guo S. Engineering the surface melt for in-space manufacturing of aluminum parts. J Mater Eng Perform 2022;31(8):6092–100.
[6] Griffiths RJ, Petersen DT, Garcia D, Yu HZ. Additive friction stir-enabled solid-state additive manufacturing for the repair of 7075 aluminum alloy. Appl Sci 2019;9(17):3486.
[7] Liu P, Liu F, Wang Y, Zhang Z, Xue P, Wu L, Zhang H, Ni D, Xiao B, Ma Z. Additive manufacturing of commercial Al–Zn–Mg–Cu aluminum alloys with mechanical properties comparable to extruded counterparts. Mater Sci Eng 2024;899:146441.
[8] Richard D, Adler PN. Calorimetric studies of 7000 series aluminum alloys: I. Matrix precipitate characterization of 7075. Metall Trans A 1977;8:1177–83.
[9] Ezatpour HR, Chaichi A, Sajjadi SA. The effect of Al2O3-nanoparticles as the reinforcement additive on the hot deformation behavior of 7075 aluminum alloy. Mater Des 2015;88:1049–56. https://doi.org/10.1016/j.matdes.2015.09.009.
[10] Tiryakioğlu M, Robinson J, Salazar-Guapuriche M, Zhao Y, Eason P. Hardness–strength relationships in the aluminum alloy 7010. Mater Sci Eng 2015;631:196–200.
[11] Bhagavatam A, Ramakrishnan A, Adapa VSK, Dinda GP. Laser metal deposition of aluminum 7075 alloy. Int J Mater Sci Res 2018;2(1):50–5. https://doi.org/10.18689/ijmsr-1000108.
[12] Messimer SL, Patterson AE, Muna N, Deshpande AP, Rocha Pereira T. Characterization and processing behavior of heated aluminum-polycarbonate composite build plates for the FDM additive manufacturing process. J Manuf Mater Proc 2018;2(1):12.
[13] Yuan Z, Tian W, Li F, Fu Q, Hu Y, Wang X. Microstructure and properties of high-entropy alloy reinforced aluminum matrix composites by spark plasma sintering. J Alloys Compd 2019;806:901–8. https://doi.org/10.1016/j.jallcom.2019.07.185.
[14] Ghasali E, Sangpour P, Jam A, Rajaei H, Shirvanimoghaddam K, Ebadzadeh T. Microwave and spark plasma sintering of carbon nanotube and graphene reinforced aluminum matrix composite. Arch Civ Mech Eng 2018;18(4):1042–54. https://doi.org/10.1016/j.acme.2018.02.006.
[15] Samal P, Vundavilli PR, Meher A, Mahapatra MM. Recent progress in aluminum metal matrix composites: a review on processing, mechanical and wear properties. J Manuf Process 2020;59:131–52.
[16] Sharma AK, Bhandari R, Aherwar A, Rimašauskienė R, Pinca-Bretotean C. A study of advancement in application opportunities of aluminum metal matrix composites. Mater Today Proc 2020;26:2419–24.
[17] Lingamurthy K, Manjunatha TH, Joshi R, Basavaraja Y, Anilkumar HM. Drilling parameters optimization and characterization of Al7075 reinforced with Al2O3. Mater Today Proc 2018;5(11):25092–101. https://doi.org/10.1016/j.matpr.2018.10.310.
[18] Ravikumar M, Reddappa H, Suresh R, Babu E, Nagaraja C. Study on Micro-nano sized Al2O3 particles on mechanical, wear and fracture behavior of Al7075 metal matrix composites. Frat Ed Integrità Strutt 2021;15(58):166–78.
[19] Aghajani S, Pouyafar V, Meshkabadi R, Volinsky AA, Bolouri A. Mechanical characterization of high volume fraction Al7075-Al2O3 composite fabricated by semisolid powder processing. J Adv Manuf Technol 2023;125(5):2569–80.
[20] Devaganesh S, Kumar PD, Venkatesh N, Balaji R. Study on the mechanical and tribological performances of hybrid SiC-Al7075 metal matrix composites. J Mater Res Technol 2020;9(3):3759–66.
[21] Karpasand F, Abbasi A, Ardestani M. Effect of amount of TiB2 and B4C particles on tribological behavior of Al7075/B4C/TiB2 mono and hybrid surface composites produced by friction stir processing. Surf Coat Technol 2020;390:125680.
[22] Abdollahi A, Nganbe M, Kabir AS. On the elimination of solidification cracks in fusion welding of Al7075 by TiC-nanoparticle enhanced filler metal. J Manuf Process 2022;81:828–36.
[23] Karimi J, Tekin M, Seefeld T. Laser metal deposition of Al 7075: effects of TiC nanoparticles. J Mater Res Technol 2024;32:3135–46.
[24] kumar Gajakosh A, Keshavamurthy R, Jagadeesha T, Kumar RS. Investigations on mechanical behavior of hot rolled Al7075/TiO2/Gr hybrid composites. Ceram Int 2021;47(10):14775–89.
[25] Ahmad S, Tian Y, Hashmi AW, Singh RK, Iqbal F, Dangi S, Alansari A, Prakash C, Chan CK. Experimental studies on mechanical properties of Al-7075/TiO2 metal matrix composite and its tribological behaviour. J Mater Res Technol 2024;30:8539–52.
[26] Sahoo BP, Das D, Chaubey AK. Strengthening mechanisms and modelling of mechanical properties of submicron-TiB2 particulate reinforced Al 7075 metal matrix composites. Mater Sci Eng 2021;825:141873.
[27] Ghazanlou SI, Eghbali B. Fabrication and characterization of GNPs and CNTs reinforced Al7075 matrix composites through the stir casting process. Int J Miner Metall Mater 2021;28:1204–14.
[28] Kurbet R, Basavaraj, Amruth C, Jayasimha S. Effect of ceramic particles on AMMC through stir casting method—a review. In: Proceedings of fourth international conference on inventive material science applications: icima 2021. Springer; 2022. p. 373–88.
[29] Venkatesh V, Deoghare AB. Fabrication and mechanical behaviour of Al-Kaoline metal matrix composite fabricated through powder metallurgy technique. Mater Today Proc 2021;38:3291–6.
[30] Chen H, Meng X, Chen J, Xie Y, Wang J, Sun S, Zhao Y, Li J, Wan L, Huang Y. Wire-based friction stir additive manufacturing. Addit Manuf 2023;70:103557.
[31] Wang J, Xie Y, Meng X, Zhao Y, Sun S, Li J, Chen J, Chen H, Ma X, Wang N. Wire-based friction stir additive manufacturing towards isotropic high-strength-ductility Al-Mg alloys. Virtual Phys Prototyp 2024;19(1):e2417369.
[32] Chen H, Zou N, Xie Y, Meng X, Ma X, Wang N, Huang Y. Wire-based friction stir additive manufacturing of AlCu alloy with forging mechanical properties. J Manuf Process 2025;133:354–66.
[33] Bagheri E, Zavari S, Adibi N, Ding H, Ghadimi H, Guo S. Additive friction stir deposition of al 7075 parts and the effect of heat treatment on microstructure, electroconductivity, and mechanical properties. J Adv Manuf Technol 2024:1–12.
[34] Yoder JK, Hahn GD, Zhao N, Brennan RE, Cho K, Yu HZ. Additive friction stir deposition-enabled upcycling of automotive cast aluminum chips. Add Manuf Lett 2023;4. https://doi.org/10.1016/j.addlet.2022.100108.
[35] Ghadimi H, Ding H, Emanet S, Talachian M, Cox C, Eller M, Guo S. Hardness distribution of Al2050 parts fabricated using additive friction stir deposition. Materials (Basel) 2023;16(3):1278.
[36] Zeng C, Ghadimi H, Ding H, Nemati S, Garbie A, Raush J, Guo S. Microstructure evolution of Al6061 alloy made by additive friction stir deposition. Materials (Basel) 2022;15(10):3676.
[37] Calvert JR. Microstructure and mechanical properties of WE43 alloy produced via additive friction stir technology. Virginia Tech; 2015.

[38] Lopez JJ, Williams MB, Rushing TW, Bikmukhametov I, Jordon JB, Allison PG, Thompson GB. Solid-state additive manufacturing of dispersion strengthened aluminum with graphene nanoplatelets. Mater Sci Eng 2024;893. https://doi.org/10.1016/j.msea.2024.146148.

[39] Patil SM, Sharma S, Joshi SS, Jin Y, Radhakrishnan M, Dahotre NB. Additive friction stir deposition of Al 6061-B4C composites: process parameters, microstructure and property correlation. Mater Sci Eng 2024;910:146840.

[40] Stubblefield G, Fraser K, Robinson T, Zhu N, Kinser R, Tew J, Cordle B, Jordon J, Allison P. A computational and experimental approach to understanding material flow behavior during additive friction stir deposition (AFSD). Comput Particle Mech 2023;10(6):1629–43.

[41] Wu B-l, Peng Y-c, Tang H-q, Meng C-c, Zhong Y-f, Zhang F-l, Zhan Y-z. Improving grain structure and dispersoid distribution of nanodiamond reinforced AA6061 matrix composite coatings via high-speed additive friction stir deposition. J Mater Process Technol 2023;317:117983.

[42] Ghadimi H, Jirandehi AP, Nemati S, Ding H, Garbie A, Raush J, Zeng C, Guo S. Effects of printing layer orientation on the high-frequency bending-fatigue life and tensile strength of additively manufactured 17-4 PH stainless steel. Materials (Basel) 2023;16(2):469.

[43] Bhandari U, Ding H, Zeng C, Yang S, Karoui A, Kim H, Zhu P, Chancey MR, Wang Y, Guo S. Study of helium irradiation effect on Al6061 alloy fabricated by additive friction stir deposition. Processes 2024;12(10):2144.

[44] Commin L, Dumont M, Masse J-E, Barrallier L. Friction stir welding of AZ31 magnesium alloy rolled sheets: influence of processing parameters. Acta Mater 2009;57(2):326–34.

[45] Rahimzadeh Ilkhichi A, Soufi R, Hussain G, Vatankhah Barenji R, Heidarzadeh A. Establishing mathematical models to predict grain size and hardness of the friction stir-welded AA 7020 aluminum alloy joints. Metall Mater Trans, B Process Metall Mater Process Sci 2014;46(1):357–65. https://doi.org/10.1007/s11663-014-0205-x.